Dalton Transactions

ROYAL SOCIETY OF CHEMISTRY

PAPER

View Article Online
View Journal

Cite this: DOI: 10.1039/d0dt03047c

Functionalised phosphonate ester supported lanthanide (Ln = La, Nd, Dy, Er) complexes†

Ingo Koehne, [a] Artur Lik,[a] Miriam Gerstel,[b] Clemens Bruhn,[a] Johann Peter Reithmaier, [b] Mohamed Benyoucef [b] and Rudolf Pietschnig *[a]

Received 31st August 2020,
Accepted 13th October 2020

DOI: 10.1039/d0dt03047c

rsc.li/dalton

A series of phosphonate ester supported lanthanide complexes bearing functionalities for subsequent immobilisation on semiconductor surfaces are prepared. Six phosphonate ester ligands (**L1–L6**) with varying aromatic residues are synthesised. Subsequent complexation with lanthanide chloride or -nitrate precursors (Ln = La, Nd, Dy, Er) affords the corresponding mono- or dimeric lanthanide model complexes $[LnX_3(\mathbf{L1–L3}$ or $\mathbf{L5–L6})_3]_n$ (X = NO_3, Cl; n = 1 (Nd, Dy, Er), 2 (La, Nd)) or $[LnCl_2Br(\mathbf{L4\text{-}Br})_2(\mathbf{L4\text{-}Cl})]_n$ (n = 1 (Nd, Dy, Er), 2 (La, Nd)) (**1–32**). All compounds are thoroughly characterised, and their luminescence properties are investigated in the visible and NIR spectral regions, where applicable.

Introduction

Lanthanide ions already find widespread application in lighting, sensing and display technologies, due to their outstanding photoluminescence properties.[1–3]

Bis-phosphonic acid ester ligands have already been successfully shown to be versatile building blocks in transition metal organic frameworks (MOFs).[4] In contrast to their carboxylic acid congeners, the key advantage of phosphonate esters originates from their lower vibrational frequencies resulting in reduced non-emissive excited state quenching and enhanced quantum yields.[5] In case of lanthanide-based coordination polymers also complexes with improved luminescence properties have been obtained.[6] Our group has focussed on this topic during the last years preparing a variety of efficiently luminescent lanthanide based MOFs.[7–9] Moreover, different poly-fluoroaryl substituted mono-[10,11] and bis-phosphanes,[12] and phosphinic acids[13] with enhanced rigidity have been prepared and investigated in terms of reactivity and coordination behaviour. Now, to obtain distinct molecular lanthanide complexes with enhanced excited state lifetimes in the context of a future attachment to semiconductor surfaces, our research focusses on preparation of aryl-substituted mono phosphonate ester ligands. A reactive functionality at the *para*-position with respect to the phosphonate substituent shall give additional access to future substitution reactions. Selected related aryl-bound mono-phosphonate esters are summarised in Chart 1. These range from differently *para*-substituted ligands **A** and **B** (X = H, Cl, Br; R = Me, Et, ^{i}Pr, ^{t}Bu),[14–16] over polyfluorinated species **C**,[17] to anthracene **D** (X = H, Cl) and 1,1′-biphenyl derivates **E** (X = H, Me).[14,18]

Results and discussion

Synthesis of ligands L1–L6

Ligands **L1**, **L2** and **L4** are prepared by straight forward Michaelis–Arbuzov[19] reactions from the corresponding benzylbromide starting materials in excellent yields of 90% and 99%

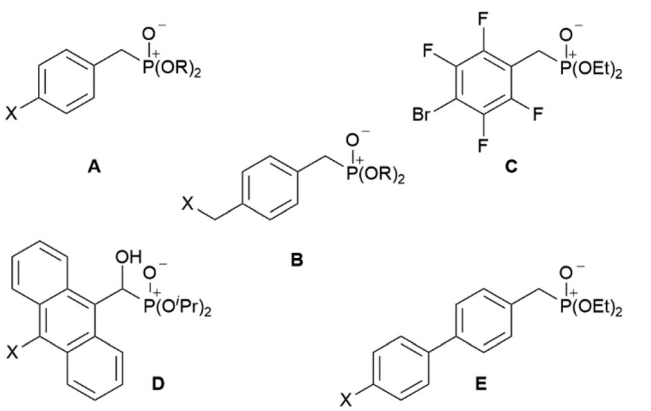

Chart 1 Selected known aryl-substituted phosphonate ester ligands **A–E**.

[a]*Institute of Chemistry and Center for Interdisciplinary Nanostructure Science and Technology (CINSaT), University of Kassel, Heinrich-Plett-Str. 40, 34132 Kassel, Germany. E-mail: pietschnig@uni-kassel.de*

[b]*Institute of Nanostructure Technologies and Analytics (INA) and CINSaT, University of Kassel, Heinrich-Plett-Str. 40, 34132 Kassel, Germany*

†Electronic supplementary information (ESI) available: Synthetic procedures & detailed spectroscopic data, NMR spectra, X-ray data, PL spectra. CCDC 2021050–2021063. For ESI and crystallographic data in CIF or other electronic format see DOI: 10.1039/d0dt03047c

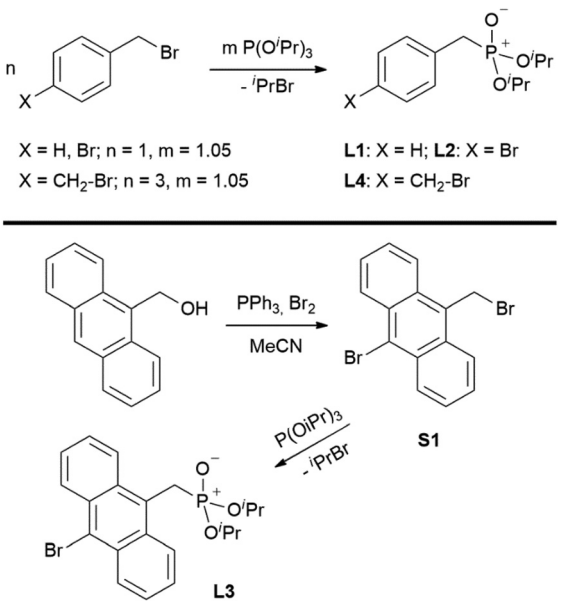

Scheme 1 Syntheses of ligands **L1**, **L2**, **L4** (top) and **L3** (bottom).

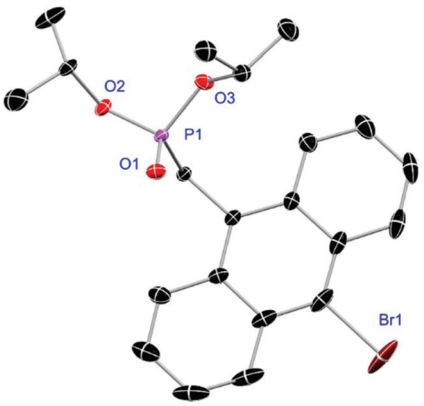

Fig. 2 Molecular structure of **L3**. Anisotropic displacement parameters are depicted at the 50% probability level. Hydrogen atoms are omitted for clarity. Structural data are given in Table 1 (*vide infra*).

for **L1** and **L2**, respectively (Scheme 1, top). **L4** is prepared according to a modified literature procedure starting from a threefold excess of 1,4-bis(bromomethyl)benzene treated with 20 h of reflux in dry toluene to promote formation of the mono-phosphorylated product.[20] **L4** is obtained in a good yield of 58% after workup. All three ligand species are obtained as colourless or pale-yellow oils. To obtain a ligand with increased bulkiness and antenna effect, anthracene-based **L3** is prepared in a two-step synthesis starting with a modified double bromination reaction of 9-(hydroxymethyl) anthracene.[21] Subsequent Michaelis–Arbuzov reaction of the obtained 9-bromo-10-(bromomethyl) anthracene (**S1**) gives **L3** as a yellow powder in an excellent overall yield of 80% (Scheme 1, bottom). Crystals suitable for SCXRD experiments were grown from vapor diffusion of pentanes into a saturated solution of **L3** in THF. **L3** crystallises in the monoclinic space group $P2_1/c$ containing one molecule in the asymmetric unit (Fig. 2). Phosphonate ester **L5** is synthesised in a good overall yield of 36% *via* a four-step procedure starting from 4,4′-dibromo-1,1′-biphenyl (Scheme 2, top; *vide infra*). The starting materials **S2**, **S3** and **S4** are prepared according to modified literature protocols.[22,23] **S4** is then phosphorylated with P(O^{i}Pr)$_3$ to give **L5** under release of ^{i}PrBr as a colourless oil which solidifies upon standing. Unfortunately, only crystals of poor quality were obtained from this solid material. Electron withdrawing substituents like fluorides are known to improve the photoluminescence properties and quantum yields of polyconjugated organic ligands and derived metal complexes due to lowered HOMO as well as LUMO energy levels and thus electron injection.[24,25] Hence, also polyfluorinated phosphonate ester ligand **L6** was prepared for subsequent lanthanide complexation (Scheme 2, bottom, *vide infra*). Compounds **S5** and **S6** are synthesised according to modified protocols.[26] Starting from pentafluoro benzaldehyde, a bromide substituent is introduced at the *para* position *via* a nucleophilic aromatic substitution to yield **S5** followed by reduction to alcohol **S6**. Subsequent bromination with PBr_3 and Michaelis–Arbuzov reaction gives **S7** and **L6**, respectively. After workup, **L6** is obtained in a good overall yield of 45% as a colourless oil which solidifies upon standing. **L6** crystallises in the triclinic space group $P\bar{1}$ hosting one molecule in the asymmetric unit. Moreover, a short intermolecular Br···O distance of only 2.77 Å is observed between the sp^2 hybridised O-atom of the phosphonate moieties and the *para* Br substituents of neighbouring molecules which remains 0.58 Å under the sum of the van der Waals radii of 3.35 Å (ref. 27) of both atoms (Fig. 1). This can only be rationalised by the formation of a so-called halogen bond for which first crystallographic evidence was provided by Hassel as early as 1954.[28,29] Here, the solid-state structure of bromine-1,4-dioxanate revealed a comparable strong intermolecular Br···O interaction with a distance of 2.71 Å. Halogen bonds are strong, specific and directional interactions including a significant charge transfer.[30] Hence, due to the short Br···O distance in **L6** the present halogen bonds can be assigned to the inner-sphere complexes of the type $[BX]^+\cdots Y^-$ according to Mulliken.[31–33] Despite that, also many analogies have been drawn between halogen- and the much weaker hydrogen bonds,[30] and many applications have been found in polymer science.[34] An intrinsic feature of the halogen bond is the $[BX]^+\cdots Y^-$ bond vector being nearly linear.[29] The corresponding C–Br···O and P═O···Br angles in **L6** of 167.4° and 166.5° deviate significantly from 180° but are in a similar range like in comparable literature structures.[35] This deviation is most likely due to a crystallographic packing effect causing the formation of an advantageous ladder-structure between adjacent molecules. Nonetheless, both angles are nearly identical classifying this interaction as a type I halogen bond.[35] In comparison to related bis-phosphonate esters (anthracene-based **I**,[9] and tetra-fluorophenyl-based **II**[36]), ligands **L3** and **L6** show comparable structural features (Table 1, *vide infra*). The P1–C1 and P1–O1 distances differ

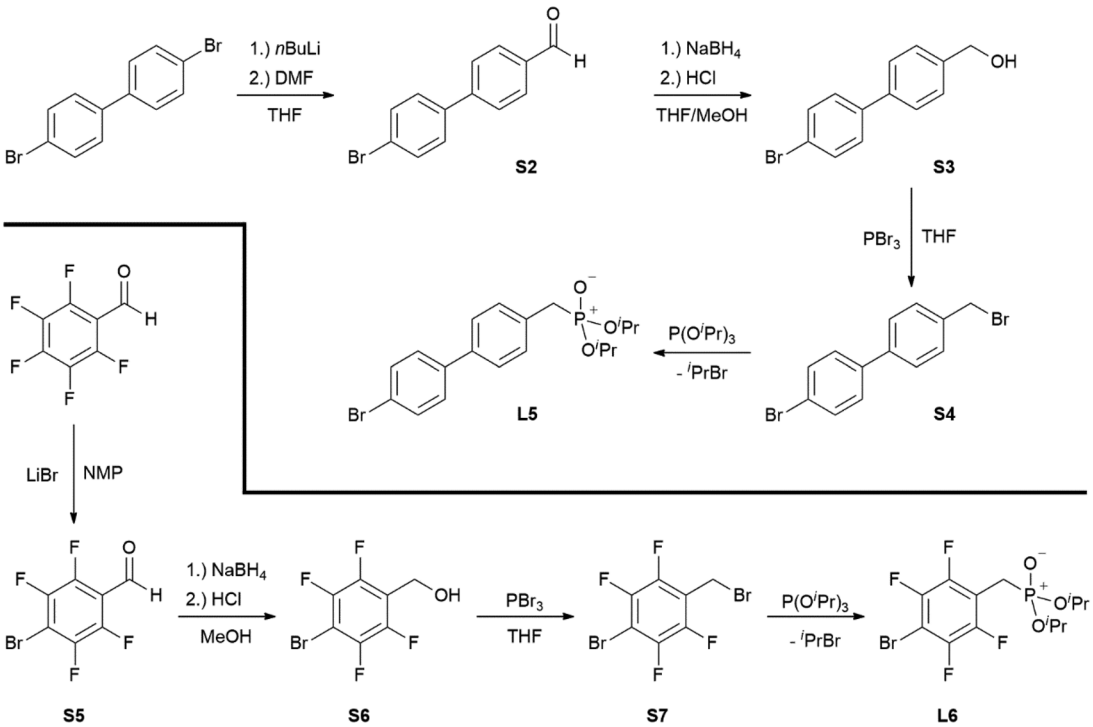

Scheme 2 Four-step preparations of phosphonate ester ligands **L5** (top) and **L6** (bottom).

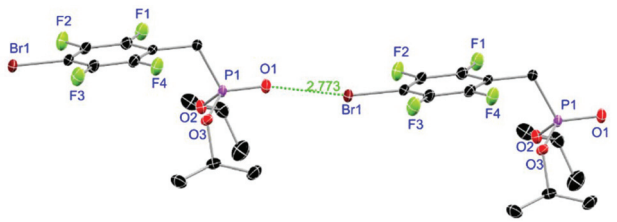

Fig. 1 Molecular structure of **L6** with schematic halogen-bond. Anisotropic displacement parameters are depicted at the 50% probability level. Hydrogen atoms are omitted for clarity. Structural data are given in Table 1.

Table 1 Selected bond lengths [Å] and angles [°] for **L3** and **L6** and related literature compounds **I** and **II**. **I** and **II** contain two molecules in the asymmetric unit thus averaged values are given

Compound	P1–C1	P1–O1	P1–C1–C2	O1–P1–C1
L3	1.805(2)	1.4679(2)	114.22(2)	116.07(1)
L6	1.803(3)	1.4653(2)	113.60(2)	112.97(1)
I	1.7978(2)	1.4633(1)	113.64(1)	115.37(1)
II	1.7900(2)	1.4690(2)	113.67(1)	113.29(8)

only marginally between 1.79–1.81 Å and 1.46–147 Å, respectively. A similar tendency can be found for the respective P1–C1–C2 and O1–P1–C1 angles. Interestingly, **L3** shows in both cases the widest ((114.22(2)° and 116.07(1)°) and **L6** the narrowest angles ((113.60(2)° and 112.97(1)°) within the row. The

Table 2 ^{31}P-NMR chemical shifts [ppm] of ligands **L1–L6** and the derived lanthanum(III) complexes **1**, **5**, **9**, **13**, **17**, **25**, **29** $[LaX_3(\mathbf{L1–L3}$ or $\mathbf{L5–L6})_3]_2$ (X = NO_3, Cl) and **21** $[LaCl_2Br(\mathbf{L4\text{-}Br})_2(\mathbf{L4\text{-}Cl})]_2$

Ligand	$[LaCl_3(\mathbf{L1–L3}$ or $\mathbf{L5–L6})_3]_2$ or $[LaCl_2Br(\mathbf{L4\text{-}Br})_2(\mathbf{L4\text{-}Cl})]_2$	$[La(NO_3)_3(\mathbf{L1–L6})_3]$
L1: 24.3	24.2	23.2
L2: 23.6	23.2	22.3
L3: 23.0	23.0	—
L4: 24.0	23.73, 23.67	—
L5: 24.4	24.0	—
L6: 19.0	19.0	—

^{31}P-NMR shifts of **L1–L6** are in-between 19.0 ppm (**L6**) and 24.4 ppm (**L5**) (Table 2) and are located within the range of related compounds found in the literature.[7–9]

Lanthanide complexes 1–32

With the desired phosphonate ester ligands **L1–L6** in hand, synthesis of derived lanthanide complexes (Ln = La, Nd, Dy, Er) is performed in EtOH starting from $[LnX_3(H_2O)_6]$ precursors (Scheme 3, *vide infra*). To have recourse to NMR spectroscopy for a proper characterisation of the products, all preparations have first been carried out with the diamagnetic La^{3+} derivative. For X = NO_3 or the use of the steric demanding anthracene-based **L3**, only three equivalents of the phosphonate esters are needed to replace all aqua ligands in the starting material and to obtain product IR spectra without residual OH-bands. In contrast, in the case of X = Cl or the less bulky **L1**, **L2**, **L4–L6**, four equivalents of the ligands are needed to

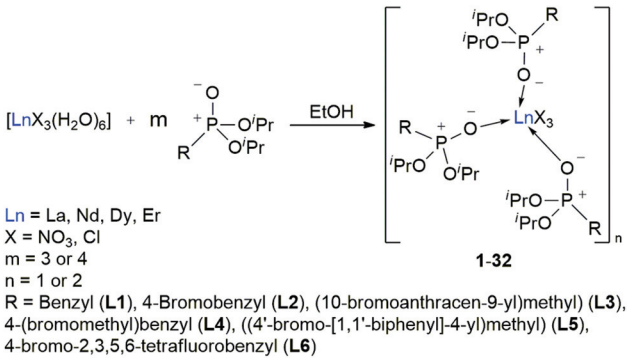

Scheme 3 Synthesis of the **L1–L6** supported lanthanide complexes **1–32**.

oust the H_2O substituents and to obtain products featuring no OH-bands in the IR spectra. For a ligand overview, see Chart 2.

After reaction, the excess of the phosphonate esters is removed by thorough extraction with pentanes so that in almost all cases mono- or dimeric complexes of the form $[LnX_3(\mathbf{L})_3]_n$ (X = NO_3, Cl, n = 1 (Nd, Dy, Er), 2 (La, Nd)) are obtained in a quantitative yield. For **L4**, complexes of the form $[LnCl_2Br(\mathbf{L4\text{-}Br})_2(\mathbf{L4\text{-}Cl})]_n$ (n = 1 (Nd, Dy, Er), 2 (La, Nd)) are found due to an Br–Cl exchange between one ligand and the lanthanide chloride precursor.

In comparison to the chlorides, the NO_3^- anions are bulkier and act as two-dentate chelate ligands. This might cause the $[LnCl_3(H_2O)_6]$ precursors to be prone to take up more than six H_2O molecules into their coordination sphere over time resulting in an aggravated permanent replacement of the water molecules. Despite of the phosphonate esters **L1–L6** being potential three-dentate chelate ligands, all obtained lanthanide complexes exhibit only a mono-dentate coordination by the oxygen atom of the P^+–O^- moieties like it is observed in related structures.[7–9] Except for the **L4**- and **L5**-supported complexes **21** and **25**, the ^{31}P-NMR signal of the free ligands experiences a 0.1–0.4 ppm shift to higher field upon complex formation with the lanthanum chloride precursors (Table 2). This effect is even more pronounced upon complexation with the lanthanum nitrates causing a high-field shift of 1.1 ppm (**1**) and 1.3 ppm (**9**), respectively. Due to a Br–Cl exchange between one ligand and the lanthanum chloride, two ^{31}P signals at 23.73 and 23.67 ppm in a ratio of 1 : 2 are observed for the **L4**-based La^{3+} complex **21**. Two sets of signals in the same ratio are also found in the corresponding ^{1}H- and ^{13}C-NMR spectra and are assigned to the two ligand modifications. Even in the MALDI-MS spectrum, aggregates with bromide as well as chloride substituted ligands are detected (see ESI†). In general, the nitrate supported complexes **1–4** and **9–12** easily solidify while most of the chloride substituted complexes tend to form viscous waxes that do not solidify or only solidify after some time. Because of that, no crystal structure determination could be carried out for the **L4**-(**21–24**) and **L5**-based complexes **25–28**.

Crystals of **L1**- and **L2**-based compounds **2**, **3**, **5**, **10**, **13** and **14** are grown from slow evaporation of saturated DCM solutions or from obtained wax-like material that crystallised after some time. The lanthanide nitrate complexes **2** (see ESI†), **3** (Fig. 3) and **10** (Fig. 4) form monomers and show a nine-fold coordination in the solid-state. Just like

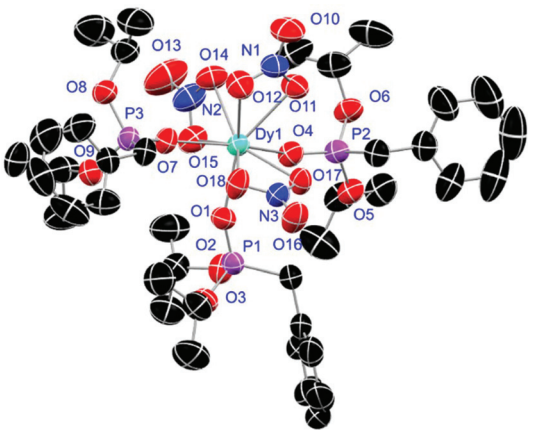

Fig. 3 Molecular structure of $[Dy(NO_3)_3(\mathbf{L1})_3]$ (**3**). Anisotropic displacement parameters are depicted at the 50% probability level. Hydrogen atoms are omitted for clarity. Structural data are given in Table 3 (*vide infra*).

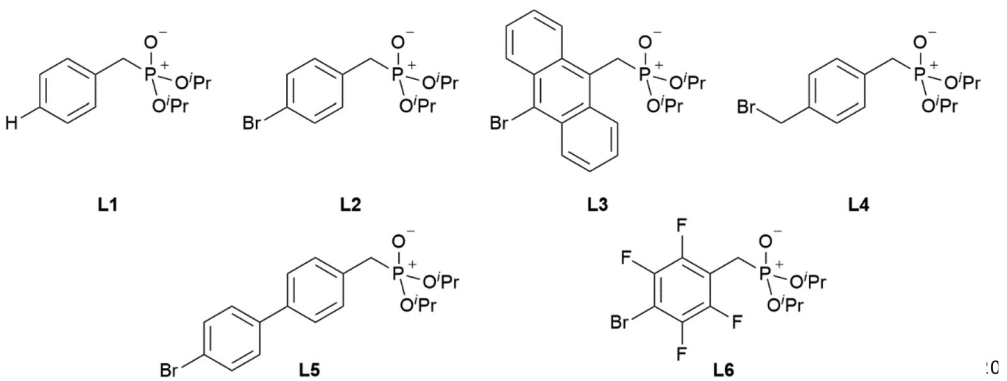

Chart 2 Overview of the phosphonate ester ligands **L1–L6** used within this work.

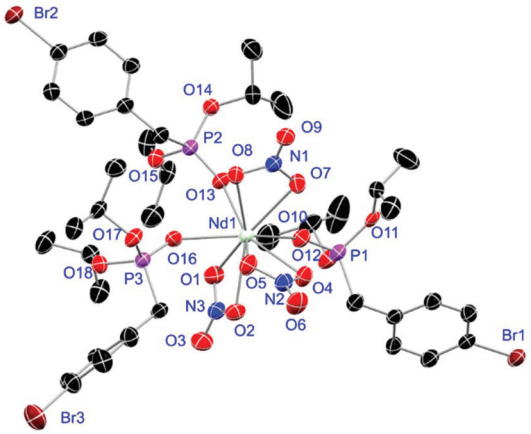

Fig. 4 Molecular structure of $[Nd(NO_3)_3(\mathbf{L2})_3]$ (**10**). Anisotropic displacement parameters are depicted at the 50% probability level. Hydrogen atoms are omitted for clarity. Structural data are given in Table 3 (*vide infra*).

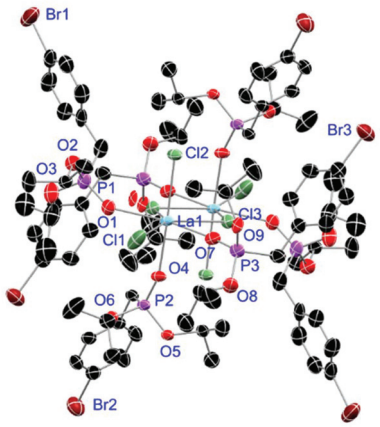

Fig. 6 Molecular structure of $[LaCl_3(\mathbf{L2})_3]_2$ (**13**). Anisotropic displacement parameters are depicted at the 50% probability level. Hydrogen atoms are omitted for clarity. Structural data are given in Table 3.

in **L6**, halogen bonds are formed in complex **10**. In this case between the bromides (Br2) and the outwards titled N═O (O9) oxygen atoms of a NO_3^- anion of adjacent molecules. In contrast to **L6**, there is less lack of electron density at the bromides thus a weaker halogen bond is formed. The O···Br distance of 3.06 Å is elongated but still shorter than the sum of the van der Waals radii of both atoms (3.35 Å (ref. 27)). The present C–Br···O angle of 169.1° is in a similar range like in **L6**. However, the N═O···Br angle of 108.3° indicates a certain perpendicular arrangement of the nitrate moiety with respect to the bromide substituent assigning this interaction rather as a type II halogen bond.[35] The **L1**- and **L2**-based lanthanide chloride compounds **5** (Fig. 5), **13** (Fig. 6) and **14** (see ESI†) show seven-fold, pentagonal-bipyramidal coordination forming chloride bridged dimers in the solid-state with an averaged M–M distance of 4.78 Å. A comparison of the **L1**- and **L2**-based Nd^{3+} nitrate complexes **2** and **10** and the La^{3+} chloride compounds **5** and **13** shows a shortening of the M–O distances in both cases when switching from **L1** to **L2** (2.381(6) (**2**) to 2.372(2) Å (**10**) and 2.433(2) (**5**) to 2.409(4) Å (**13**)). The same trend can be seen for the M–Cl distances of the non-bridging chlorides in **5** and **13** (2.821(6) to 2.750(2) Å) while the bond length of the bridging chlorides (2.924(6) to 2.914(2) Å) seems to be less effected by an increasing steric demand of the ligand periphery in **L2**. Apparently contrary trends are obtained for the P^+–O^- distances and the M–O–P angles. The P^+–O^- bond length in **2** and **10** is unaffected while the M–O–P angle is slightly narrowed from 154.6(4)° in **2** to 152.4(2)° in complex **10**. In contrast, the P^+–O^- distance decreases from 1.486(2) Å in **5** to 1.463(5) Å in **10** while the M–O–P angle is significantly increased from 151.3(1)° to 159.4(3)°.

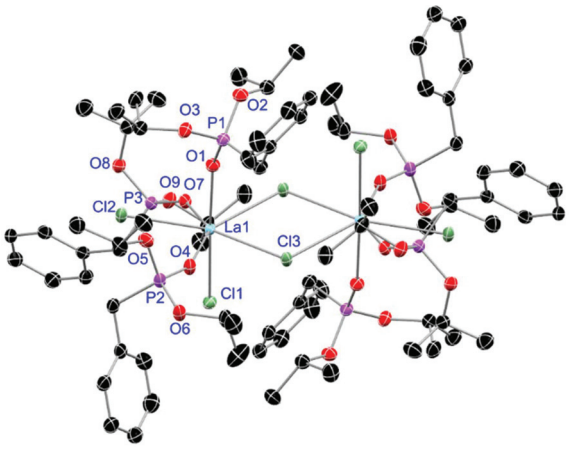

Fig. 5 Molecular structure of $[LaCl_3(\mathbf{L1})_3]_2$ (**5**). Anisotropic displacement parameters are depicted at the 50% probability level. Hydrogen atoms are omitted for clarity. Structural data are given in Table 3 (*vide infra*).

For the **L3**-based complexes, crystals suitable for X-ray diffraction experiments could only be obtained from saturated EtOH solutions at −20 °C (**17**–**19**) or from vapor diffusion of pentanes into a saturated THF solution (**20**). Just like complexes **5**, **13** and **14**, compound **17** shows a seven-fold coordination forming a chloride bridged dimer in the solid-state (Fig. 7, *vide infra*). Owing to the increased steric demand of **L3**, it is most likely that the preferred dimer formation only can occur upon exchange of an equivalent **L3** with an EtOH molecule per La^{3+} ion. Complex **18** also shows a seven-fold pentagonal-bipyramidal coordination but forms a monomer because of three attached bulky molecules of **L3** (Fig. 8, *vide infra*). Since all obtained products show no residual OH-bands in the IR spectrum, the additionally attached H_2O molecule to suit the coordination sphere of the Nd^{3+} cation has to origin from airborne water during the crystallisation process. Just like in **17**, a phosphonate ester **L3** is substituted by an EtOH molecule in complex **19** (Fig. 9). A monomeric octahedral coordination is most likely preferred due to the smaller ionic radius of the Dy^{3+} ion. The same coordination mode can be observed for complex **20** (Fig. 10). The coordination sphere is made up by three chloride anions and three **L3** oxygen atoms.

Table 3 Selected bond lengths [Å] and angles [°] of **L1**-based complexes **2**, **3**, **5**, **L2**-based **10**, **13**, **14**, **L3**-based **17–20** and **L6**-based **31** and **32**. Distances to solvent oxygen atoms are not considered

Complex	M–O/M–$O_{(NO_3)}$	M–Cl/M–(μ-Cl)	P^+–O^-	M–O–P
$[Nd(NO_3)_3(\mathbf{L1})_3]$ (**2**)	2.381(6)/2.531(6)	—	1.483(7)	154.6(4)
$[Dy(NO_3)_3(\mathbf{L1})_3]$ (**3**)	2.297(2)/2.455(2)	—	1.476(2)	155.6(1)
$[LaCl_3(\mathbf{L1})_3]_2$ (**5**)	2.433(2)	2.821(6)/2.924(6)	1.486(2)	151.3(1)
$[Nd(NO_3)_3(\mathbf{L2})_3]$ (**10**)	2.372(2)/2.538(2)	—	1.483(3)	152.4(2)
$[LaCl_3(\mathbf{L2})_3]_2$ (**13**)	2.409(4)	2.750(2)/2.914(2)	1.463(5)	159.4(3)
$[NdCl_3(\mathbf{L2})_3]_2$ (**14**)	2.378(9)	2.725(3)/2.910(3)	1.480(9)	160.2(6)
17 as $[LaCl_3(\mathbf{L3})_2(EtOH)]_2$·EtOH	2.421(3)	2.802(1)/2.873(1)	1.483(3)	149.2(2)
18 as $[NdCl_3(\mathbf{L3})_3(H_2O)]$	2.378(4)	2.764(1)	1.483(4)	147.9(2)
19 as $[DyCl_3(\mathbf{L3})_2(EtOH)]$·2EtOH	2.253(3)	2.612(1)	1.489(3)	153.1(2)
$[ErCl_3(\mathbf{L3})_3]$ (**20**)	2.230(4)	2.616(1)	1.493(4)	150.1(3)
31 as $[DyCl_2(\mathbf{L6})_3(H_2O)]Cl$	2.256(6)	2.574(3)	1.477(6)	167.0(4)
32 as $[ErCl_2(\mathbf{L6})_3(H_2O)]Cl$	2.209(6)	2.521(2)	1.457(6)	166.9(4)

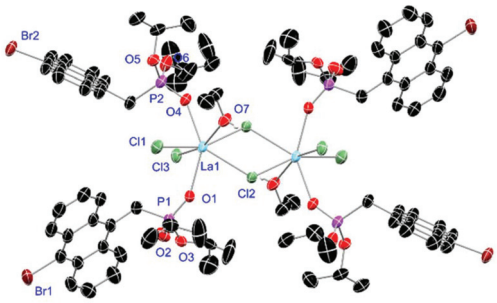

Fig. 7 Molecular structure of **17**, crystallised as $[LaCl_3(\mathbf{L3})_2(EtOH)]_2$·EtOH. Anisotropic displacement parameters are depicted at the 50% probability level. Except for freely refined hydrogens, these and a co-crystallised EtOH molecule are omitted for clarity. Structural data are given in Table 3.

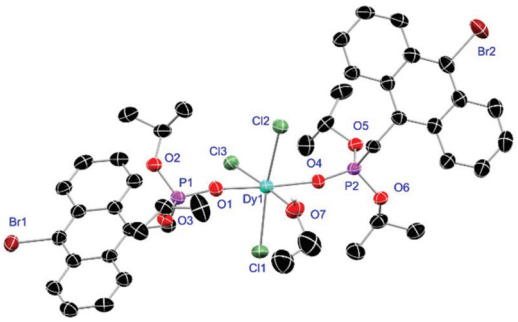

Fig. 9 Molecular structure of **19**, crystallised as $[DyCl_3(\mathbf{L3})_2(EtOH)]$·2EtOH. Anisotropic displacement parameters are depicted at the 50% probability level. Except for freely refined hydrogens, these and two co-crystallised EtOH molecules are omitted for clarity. Structural data are given in Table 3.

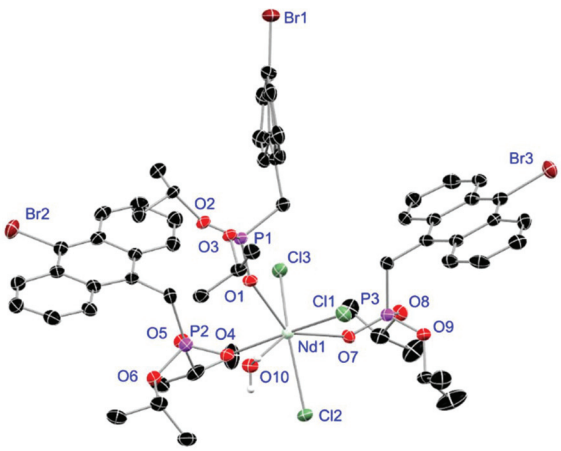

Fig. 8 Molecular structure of **18**, crystallised as $[NdCl_3(\mathbf{L3})_3(H_2O)]$. Anisotropic displacement parameters are depicted at the 50% probability level. Except for freely refined hydrogens, these are omitted for clarity. Structural data are given in Table 3.

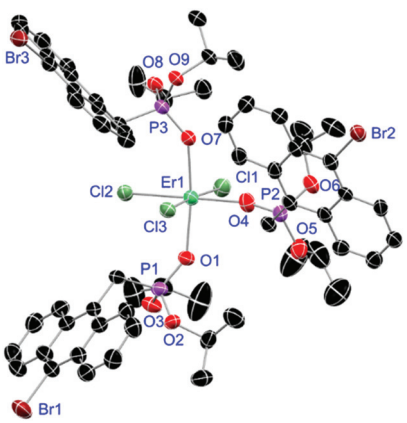

Fig. 10 Molecular structure of $[ErCl_3(\mathbf{L3})_3]$ (**20**). Anisotropic displacement parameters are depicted at the 50% probability level. Hydrogen atoms and a co-crystallised THF molecule are omitted for clarity. Structural data are given in Table 3.

Consistent with a step-wise decrease of the effective ionic radii of the cations: La^{3+} (103 pm) > Nd^{3+} (98 pm) > Dy^{3+} (91 pm) > Er^{3+} (89 pm),[37] the M–O and M–Cl distances are successively decreasing from 2.421(3) Å and 2.802(1) Å in **17**, over 2.378(4) Å and 2.764(1) Å (**18**) and 2.253(3) Å and 2.612(1) Å (**19**) to 2.230(4) Å and 2.616(1) Å in complex **20**. The P^+–O^- bond lengths show a contrasting trend by slightly increasing from 1.483(3) Å in **17** to 1.493(4) Å in **20**. Moreover, the acutest

M–O–P angles amongst all synthesised complexes are found in **17** (149.2(2)°) and **18** (147.9(2)°).

Complexes **31** and **32** are obtained as slowly crystallising waxes. They are isostructural and crystallise as pseudo-octahedrally coordinated monomers (Fig. 11). A chloride anion is replaced by a water substituent in both molecules resulting in the Cl^- to function now as counterion forming a partially solvent separated ion pair. Just like in complex **18**, the IR spectra of both complexes show no residual OH-bands after workup. In contrast to the free ligand **L6**, no halogen bonds are formed between the complex molecules in **31** and **32** due to the phosphonate esters now donating electron density towards the lanthanide cations. On the one hand, both compounds show with 2.256(6), 2.574(3) and 1.477(6) Å (**31**) and 2.209(6), 2.521(2) and 1.457(6) Å (**32**) the shortest M–O, M–Cl and P^+–O^- distances among the crystallised complexes. On the other hand, this automatically causes the widest M–O–P angles of 167.0(4)° (**31**) and 166.9(4)° (**32**), respectively.

Solid-state absorption properties

The absorption spectra of complexes **1–32** in the range of 300–850 nm essentially look the same showing expected sharp absorption bands of the Nd^{3+} ($\lambda_{abs,\ max}$ = 584 nm), Dy^{3+} ($\lambda_{abs,\ max}$ = 811 nm) and Er^{3+} ($\lambda_{abs,\ max}$ = 526 nm) cations, respectively. Some exemplary spectra of complexes **2** (black), **3** (orange) and **4** (blue) are summarised in Fig. 12 indicating all three cations to share an absorption around 800 nm (for detailed data, see ESI†). The obtained spectra only differ by an either more or less strong ligand absorption in the blue region that is most pronounced for the **L3**-based complexes **17–20**.

Emission properties of the Dy^{3+} complexes

Owing to Laporte-forbidden 4f–4f-transitions, all complexes are expected to show no or only weak metal emissions. An applied excitation at 366 nm affords only in case of the Dy^{3+} compounds sharp emission bands in the range of 300–850 nm. Nonetheless, the Dy^{3+} nitrate based complexes **3** and **11** exhibit relatively strong white light emission of the cation with quantum yields of 9% and 13%, respectively which

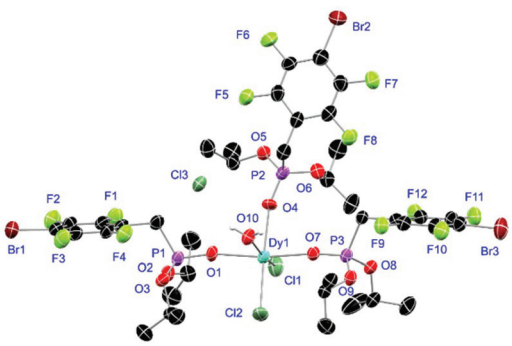

Fig. 11 Molecular structure of **31**, crystallised as $[DyCl_2(\mathbf{L6})_3(H_2O)]Cl$. Anisotropic displacement parameters are depicted at the 50% probability level. Except for freely refined hydrogens, these are omitted for clarity. Structural data are given in Table 3 (*vide supra*).

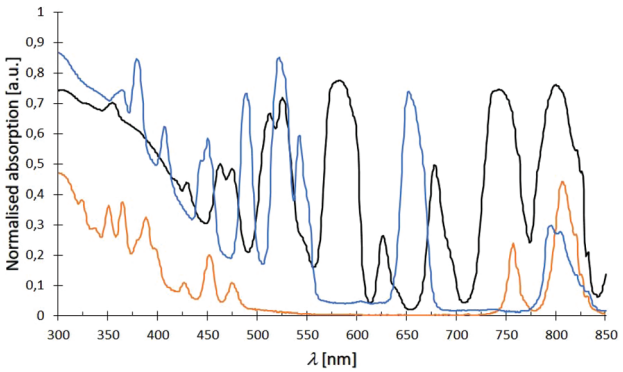

Fig. 12 Examplary normalised absorption spectra of complexes $[Nd(NO_3)_3(\mathbf{L1})_3]$ (**2**) (black), $[Dy(NO_3)_3(\mathbf{L1})_3]$ (**3**) (orange) and $[Er(NO_3)_3(\mathbf{L1})_3]$ (**4**) (blue) at room temp. with typically sharp Nd^{3+}, Dy^{3+} and Er^{3+} absorption bands.

is most likely due to a ligand-to-metal energy transfer (Fig. 13(a)). In turn, the obtained Dy^{3+} chloride-based complexes **7**, **15**, **19**, **23**, **27** and **31** show the expected very weak emissions with no evidence for bands affiliated to ligand-to-metal energy transfer or modified ligand emission. This indicates an enhanced stabilisation of long living excited states within the latter systems. The only difference between the nitrate- and chloride-based Dy^{3+} complexes is the anions themselves. Hence, this deviating luminescence behaviour can only be rationalised by the NO_3^- anions promoting a ligand-to-metal energy transfer and fast fluorescence processes. In general, the emission spectrum of anthracene ligand **L3**-based complex **19** is dominated by the weak but broad ligand emission between 450–650 nm (blue to green) covering most of the metal emissions (Fig. 13(b)). The emission spectra of the Dy^{3+} chloride complexes **7**, **15**, **23** and **31** supported by ligands **L1**, **L2**, **L4** and **L6**, respectively are very similar exhibiting very weak to weak ligand emissions between 400 to 550 nm and some of the weak Dy^{3+} emission bands can be assigned (Fig. 13(c), *vide infra*). The spectrum of complex **27** is dominated by a very strong emission of the 1,1′-biphenyl-based phosphonate **L5** between 400–550 nm (blue) covering the $^4F_{9/2} \rightarrow {}^6H_{15/2}$ emission band of the cation (Fig. 13(d)). After enlargement of the area between 550–850 nm, still some of the remaining, weak Dy^{3+} emissions could be visualised and assigned.

Emission properties of the Nd^{3+} complexes

The luminescence properties of **L2**, **L3**; **L5** and **L6** supported Nd^{3+} chloride-based complexes **14**, **18**, **26** and **30** are investigated using micro-photoluminescence (μ-PL) spectroscopy. The emission spectra feature the characteristic transitions of the Nd^{3+} ion in the NIR region (Fig. 14). Three narrow emission bands are illustrated which are centred at *ca.* 890, 1060 and 1320 nm, that correspond to the $^4F_{3/2} \rightarrow {}^4I_{9/2}$, $^4F_{3/2} \rightarrow {}^4I_{11/2}$ and $^4F_{3/2} \rightarrow {}^4I_{13/2}$ transitions, respectively. The band at 1060 nm is predominant in all four cases. Interestingly, only complex **14** (Fig. 14(a)) exhibits a distinct signal splitting of

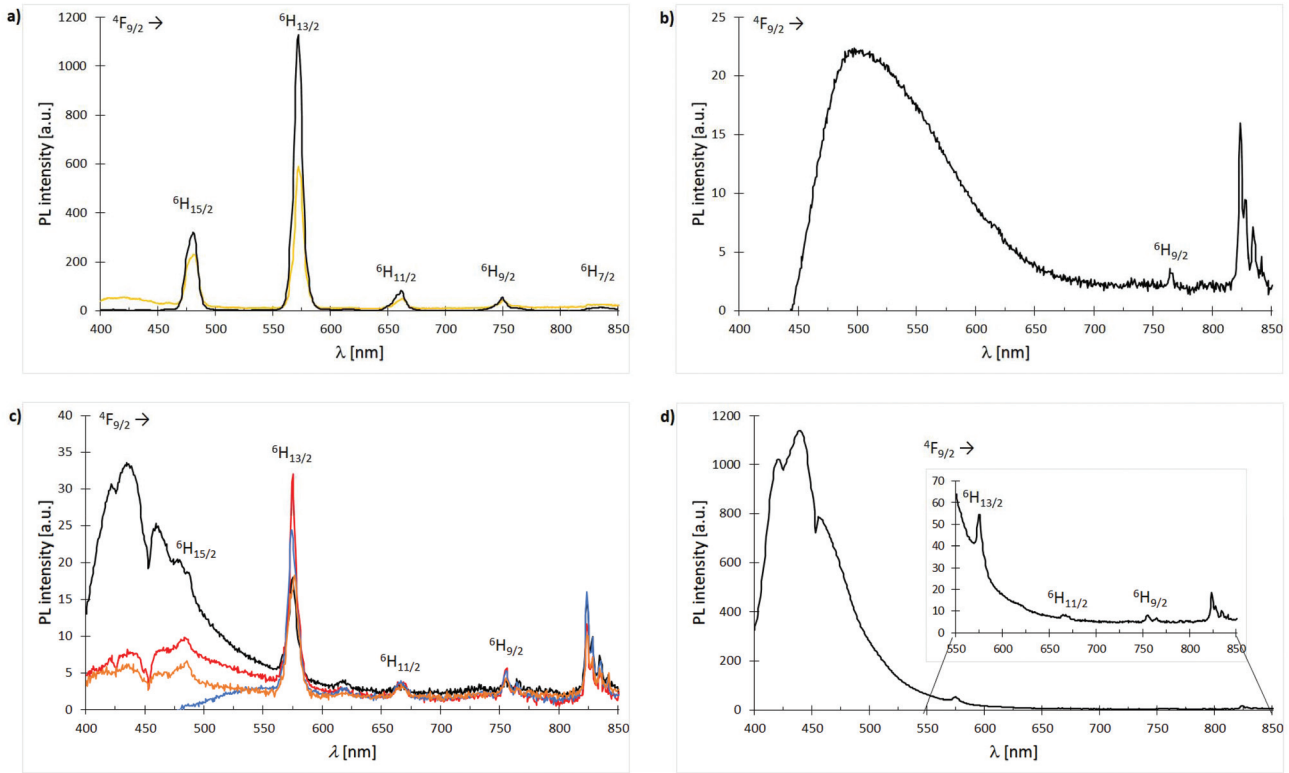

Fig. 13 Emission spectra (λ_{exc} = 366 nm) of Dy^{3+} complexes **3**, **7**, **11**, **15**, **19**, **23**, **27** and **31** at room temp.: (a) spectra overlay of complexes [Dy$(NO_3)_3$(**L1**)$_3$] (**3**) (bright orange) and [Dy$(NO_3)_3$(**L2**)$_3$] (**11**) (black); (b) spectrum of complex [$DyCl_3$(**L3**)$_3$] (**19**); (c) spectra overlay of complexes [$DyCl_3$(**L1**)$_3$] (**7**) (black), [$DyCl_3$(**L2**)$_3$] (**15**) (red), [$DyCl_2$Br(**L4-Br**)$_2$(**L4-Cl**)] (**23**) (blue) and [$DyCl_3$(**L6**)$_3$] (**31**) (dark orange); (d) spectrum of complex [$DyCl_3$(**L5**)$_3$] (**27**).

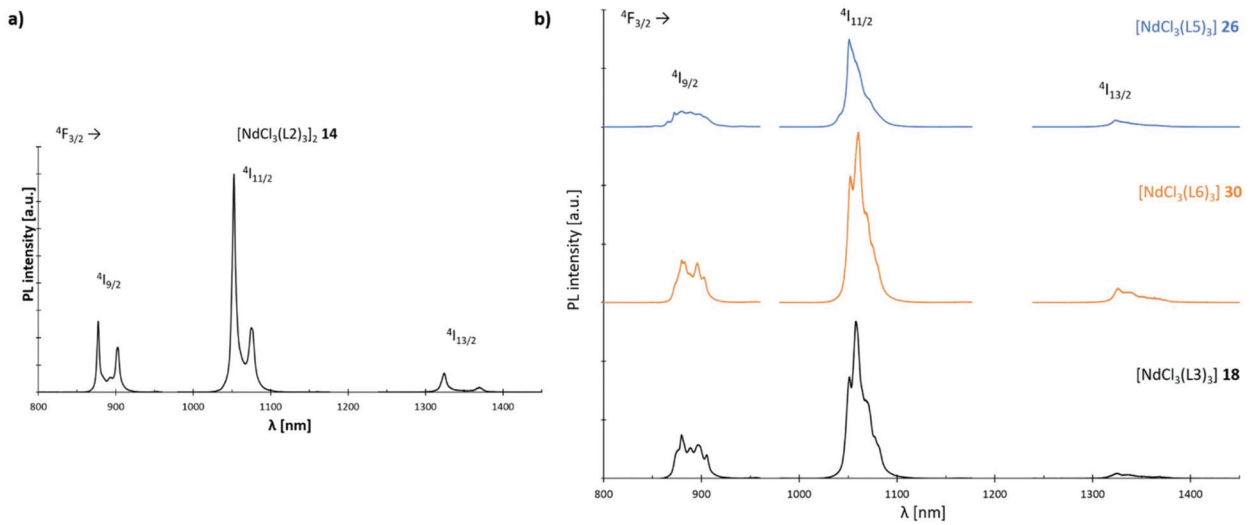

Fig. 14 Emission spectra (λ_{exc} = 750 nm) of Nd^{3+} complexes **14**, **18**, **26** and **30** at room temp.: (a) spectrum of complex [$NdCl_3$(**L2**)$_3$]$_2$ (**14**); (b) stacked spectra of complexes [$NdCl_3$(**L3**)$_3$] (**18**) (black), [$NdCl_3$(**L5**)$_3$] (**26**) (blue) and [$NdCl_3$(**L6**)$_3$] (**30**) (orange).

25 nm ($^4F_{3/2} \rightarrow {}^4I_{9/2}$, $^4F_{3/2} \rightarrow {}^4I_{11/2}$) and 47 nm ($^4F_{3/2} \rightarrow {}^4I_{13/2}$), respectively in its PL-spectrum. This feature is most likely due to a preferential formation of dimeric structures in **L2**-based **14** resulting in a Nd–Nd distance of 4.80 Å. Electrostatic ligand–metal interactions are known to influence lanthanide ion f-shell electrons,[38] and as a result to affect their fluorescence response.[39–41] In a recent study by Guillou *et al.*, a similar splitting was observed for Eu^{3+} clusters and tentatively

assigned to electronic orbital interactions between f-orbitals of the rare-earth metal centres and, in the case of this cluster, the oxygen-centred orbitals of an adjacent oxo-ligand.[42] Such an electrostatic ligand effect could also be observed for the electronic structure of a variety of mono-lanthanide species by Furet *et al.*[38] Hence, the less pronounced splitting in the monomeric complexes **18**, **26** and **30** can most likely be assigned as well to such a type of interaction.

Experimental section

X-ray diffraction experiments were performed with either a STOE IPDS 2 with an image plate (Ø 34 cm) using a Mo-GENIX source (λ = 0.71073 nm) or a STOE StadiVari instrument with DECTRIS PILATUS 200 K using a Mo-GENIX source (λ = 0.71073 nm). All structures were solved using the dual space method (SHELXT)[43] and were refined against F2 with SHELXL[44] or OLEX2.[45] Additional programs used for structural analysis include Mercury[46] and Platon.[47] CCDC 2021050–2021063† contain the supplementary crystallographic data for this paper.

For μ-PL experiments, the laser (λ_{exc} = 750 nm) is focused on the complexes by a microscope objective (NA = 0.7) to a spot size of ~1 μm. The same objective was used to collect the emission from the complexes. The luminescence is then spectrally filtered by a 0.75 m focal length spectrometer equipped with liquid nitrogen-cooled CCD and InGaAs detectors. The μ-PL spectra were taken at room temperature with a laser excitation power of 6 mW.

Conclusions

The preparation of six phosphonate ligand systems (**L1–L6**) carrying differently substituted aryl residues as well as of 32 derived lanthanide complexes (**1–32**) has been presented. For **L1**, **L2** and **L4** modified literature known procedures are introduced while phosphonates **L3**, **L5** and **L6** represent completely new ligand systems with an additional bromo functionality for further functionalisation. As a highlight, the tetrafluoro aryl substituted phosphonate **L6** shows a unique two-dimensional type I halogen bond network in the solid-state. Substitution reactions with $[LnX_3(H_2O)_6]$ (Ln = La, Nd, Dy, Er; X = NO_3^-, Cl^-) precursor compounds in EtOH yielded the derived model complexes of the form $[LnX_3(\mathbf{L1–L3}$ or $\mathbf{L5–L6})_3]_n$ (X = NO_3, Cl; n = 1 (Nd, Dy, Er), 2 (La, Nd)) or $[LnCl_2Br(\mathbf{L4\text{-}Br})_2(\mathbf{L4\text{-}Cl})]_n$ (n = 1 (Nd, Dy, Er), 2 (La, Nd)) which have been thoroughly characterised. Unfortunately, not all the obtained crystal structures obey to this formula due to additional solvent coordination accompanied by partial ligand replacement during the crystallisation process. The obtained crystal structures show the lanthanide nitrate-based ones to form monomers in the solid-state. The lanthanide chloride-based compounds preferably form chloride bridged dimers for the bigger La^{3+} cation and the less sterically demanding phosphonates **L1**, **L2** and **L6**, and tend to form monomers in case of the smaller Dy^{3+} and Er^{3+} ions and the bulky anthracene-based ligand **L3**. For the medium sized Nd^{3+}, monomeric as well as dimeric species are observed. Moreover, compound $[Nd(NO_3)_3(\mathbf{L2})_3]$ (**10**) is the only complex within this work to show the formation of a two-dimensional halogen bond network in the solid-state which was assigned to a type II halogen bond interaction due to a more perpendicular arrangement of the respective moiety. Absorption spectra of complexes **1–32** have been recorded showing the expected sharp lanthanide absorption bands in all cases. The recording of emission spectra (λ_{exc} = 366 nm) of the obtained Dy^{3+} model compounds shows the respective nitrate-based derivatives **3** and **11** to exhibit a relatively strong white metal emission with quantum yields of 9% and 13%, respectively. In contrast, the chloride-based complexes show only very weak emissions at this excitation wavelength. Without speculation potential reasons for this behaviour must remain elusive until more detailed studies such as excited state lifetime measurements along with quantum chemical calculations shed more light on this issue in the future. The recorded μ-PL-spectra (λ_{exc} = 750 nm) of the Nd^{3+} chloride-based complexes **14**, **18**, **26** and **30** exhibit a similar behaviour showing weak metal emissions in the NIR region. Nonetheless, interesting splitting features tentatively assigned to electronic orbital interactions between f-orbitals of the Nd^{3+} centres and the oxygen-centred orbitals of adjacent oxo-ligands are observed.

Conflicts of interest

The authors declare no competing financial interest.

Acknowledgements

The federal state of Hesse, Germany is kindly acknowledged for financial support of the SMolBits project within the LOEWE program.

Notes and references

1 O. Guillou, C. Daiguebonne, G. Calvez and K. Bernot, *Acc. Chem. Res.*, 2016, **49**, 844–856.
2 J.-C. Bünzli, *Nat. Chem.*, 2010, **2**, 696–696.
3 B. Samson, A. Carter and K. Tankala, *Nat. Photonics*, 2011, **5**, 466–467.
4 J.-W. Zhang, C.-C. Zhao, Y.-P. Zhao, H.-Q. Xu, Z.-Y. Du and H.-L. Jiang, *CrystEngComm*, 2014, **16**, 6635–6644.
5 Y. Hasegawa, Y. Kimura, K. Murakoshi, Y. Wada, J.-H. Kim, N. Nakashima, T. Yamanaka and S. Yanagida, *J. Phys. Chem.*, 1996, **100**, 10201–10205.
6 L. Zhang, W. Dou, W. Liu, C. Xu, H. Jiang, C. Chen, L. Guo, X. Tang and W. Liu, *Inorg. Chem. Commun.*, 2015, **59**, 53–56.

7 K. Krekić, E. Käkel, D. Klintuch, D. Bloß and R. Pietschnig, *Z. Anorg. Allg. Chem.*, 2018, **644**, 149–154.
8 K. Krekić, D. Klintuch and R. Pietschnig, *Chem. Commun.*, 2017, **53**, 11076–11079.
9 K. Krekić, D. Klintuch, C. Lescop, G. Calvez and R. Pietschnig, *Inorg. Chem.*, 2019, **58**, 382–390.
10 A. Orthaber, M. Fuchs, F. Belaj, G. N. Rechberger, C. O. Kappe and R. Pietschnig, *Eur. J. Inorg. Chem.*, 2011, **2011**, 2588–2596.
11 A. Orthaber, F. Belaj and R. Pietschnig, *J. Organomet. Chem.*, 2010, **695**, 974–980.
12 A. Orthaber, F. Belaj, J. H. Albering and R. Pietschnig, *Eur. J. Inorg. Chem.*, 2010, **2010**, 34–37.
13 A. Orthaber, J. H. Albering, F. Belaj and R. Pietschnig, *J. Fluor. Chem.*, 2010, **131**, 1025–1031.
14 T. Huang, T. Chen and L.-B. Han, *J. Org. Chem.*, 2018, **83**, 2959–2965.
15 K. Baczko, W.-Q. Liu, B. P. Roques and C. Garbay-Jaureguiberry, *Tetrahedron*, 1996, **52**, 2021–2030.
16 P. Li, M. Zhang, M. L. Peach, H. Liu, D. Yang and P. P. Roller, *Org. Lett.*, 2003, **5**, 3095–3098.
17 H. C. Li, Y. P. Lin, P. T. Chou, Y. M. Cheng and R. S. Liu, *Adv. Funct. Mater.*, 2007, **17**, 520–530.
18 B. A. Arbuzov, V. M. Zoroastrova and G. A. Tudril, *Izvestiya Akademii Nauk SSSR*, Seriya Khimicheskaya, 1970, pp. 90–95.
19 A. E. Arbuzov, *J. Russ. Phys.-Chem. Soc.*, 1906, **38**, 687–671.
20 B. Moreau, P.-A. Jaffrès and D. Villemin, *Org. Prep. Proced. Int.*, 2002, **34**, 549–552.
21 J. H. Clements and S. E. Webber, *J. Phys. Chem. B*, 1999, **103**, 9366–9377.
22 F. Leroux, T. U. Hutschenreuter, C. Charrière, R. Scopelliti and R. W. Hartmann, *Helv. Chim. Acta*, 2003, **86**, 2671–2686.
23 H. Sato, J. A. Bender, S. T. Roberts and M. J. Krische, *J. Am. Chem. Soc.*, 2018, **140**, 2455–2459.
24 F. Babudri, G. M. Farinola, F. Naso and R. Ragni, *Chem. Commun.*, 2007, 1003–1022.
25 Y. Hattori, T. Kusamoto, T. Sato and H. Nishihara, *Chem. Commun.*, 2016, **52**, 13393–13396.
26 A. Franzke and A. Pfaltz, *Synthesis*, 2008, 245–252.
27 A. Bondi, *J. Phys. Chem.*, 1964, **68**, 441–451.
28 O. Hassel and J. Hvoslef, *Acta Chem. Scand.*, 1954, **8**, 873.
29 O. Hassel, *Science*, 1970, **170**, 497–502.
30 A. C. Legon, *Angew. Chem., Int. Ed.*, 1999, **38**, 2686–2714.
31 R. S. Mulliken, *J. Phys. Chem.*, 1952, **56**, 801–822.
32 R. S. Mulliken, *J. Am. Chem. Soc.*, 1952, **74**, 811–824.
33 R. S. Mulliken, *J. Am. Chem. Soc.*, 1950, **72**, 600–608.
34 G. Berger, J. Soubhye and F. Meyer, *Polym. Chem.*, 2015, **6**, 3559–3580.
35 L. Brammer, G. Mínguez Espallargas and S. Libri, *CrystEngComm*, 2008, **10**, 1712–1727.
36 F. C. Krebs and T. Jensen, *J. Fluor. Chem.*, 2003, **120**, 77–84.
37 R. D. Shannon, *Acta Crystallogr., Sect. A: Cryst. Phys., Diffr., Theor. Gen. Crystallogr.*, 1976, **32**, 751–767.
38 E. Furet, K. Costuas, P. Rabiller and O. Maury, *J. Am. Chem. Soc.*, 2008, **130**, 2180–2183.
39 D. Van der Voort, G. J. Dirkens and G. Blasse, *J. Phys. Chem. Solids*, 1992, **53**, 219–225.
40 D. Parker, R. S. Dickins, H. Puschmann, C. Crossland and J. A. K. Howard, *Chem. Rev.*, 2002, **102**, 1977–2010.
41 S. K. Mahesh, P. P. Rao, M. Thomas, T. L. Francis and P. Koshy, *Inorg. Chem.*, 2013, **52**, 13304–13313.
42 F. Le Natur, G. Calvez, J.-P. Guégan, L. Le Pollès, X. Trivelli, K. Bernot, C. Daiguebonne, Ch. Neaime, K. Costuas, F. Grasset and O. Guillou, *Inorg. Chem.*, 2015, **54**, 6043–6054.
43 G. M. Sheldrick, *Acta Crystallogr., Sect. A: Found. Adv.*, 2015, **71**, 3–8.
44 G. Sheldrick, *Acta Crystallogr., Sect. C: Struct. Chem.*, 2015, **71**, 3–8.
45 O. V. Dolomanov, L. J. Bourhis, R. J. Gildea, J. A. K. Howard and H. Puschmann, *J. Appl. Crystallogr.*, 2009, **42**, 339–341.
46 C. F. Macrae, I. Sovago, S. J. Cottrell, P. T. A. Galek, P. McCabe, E. Pidcock, M. Platings, G. P. Shields, J. S. Stevens, M. Towler and P. A. Wood, *J. Appl. Crystallogr.*, 2020, **53**, 226–235.
47 A. Spek, *Acta Crystallogr., Sect. D: Biol. Crystallogr.*, 2009, **65**, 148–155.